Optics & Laser Technology 169 (2024) 110120

Contents lists available at ScienceDirect

Optics and Laser Technology

journal homepage: www.elsevier.com/locate/optlastec

Full length article

Damage evolution and crystalline orientation effects in ultrafast laser micro/nano processing of single-crystal diamond

Huili Han, Minglin He, Hao Liu, Bi Zhang *, Cong Zhou

Department of Mechanical and Energy Engineering, Southern University of Science and Technology, Shenzhen 518055, China

ARTICLE INFO

Keywords:
Ultrafast laser
Single-crystal diamond
Laser-induced damage
Crystal orientation
Micro/nano processing

ABSTRACT

Single-crystal diamond is a typical difficult-to-machine material because of its extreme hardness and high brittleness. Compared with traditional machining techniques, ultrafast laser is believed to enable materials processing with high efficiency, high quality and high spatial resolution. To understand the formation mechanism and crystalline orientation effects of damage in ultrafast laser processing diamond, single-path scans were performed in different crystal directions, and groove shape, surface morphology, subsurface damage, phase transformation, and laser-induced periodic surface structure (LIPSS) were systematically analyzed. The experimental results illustrate that the damage evolution can be divided into three different stages according to the pulse number, named weak ablation stage, severe cracking stage, and severe phase transformation stage. Crystal orientation significantly affects the groove shapes, cracks, and phase transformation, and these differences are related to the cleavage energy and atomic rearrangement energy of the crystal plane deposited by the laser energy during processing. At low pulse numbers, the surface graphitization is initiated easier along the <110> direction, which makes the absorption rate of laser energy locally enhanced, further driving the anisotropy of the processing damage at moderate and high pulse numbers. This work provides a new perspective on ultrafast laser processing of single-crystal diamond, which is crucial for ultra-precision and low-damage fabrication of diamond-based functional micro/nano devices.

1. Introduction

Single-crystal diamond is widely used to fabricate ultraprecision cutting tools, heat dissipation components, optical windows, and semiconductor devices, due to its excellent physical and chemical properties. However, single-crystal diamond is difficult to machine into target morphologies owing to its extreme hardness, high brittleness, and low fracture toughness, which significantly limits the application of diamond devices. Recently, ultrafast laser processing technique (pulses shorter than a few tens of picoseconds) has been rapidly developed. This technique has a series of advantages, such as high machining quality, a small heat-affected zone, low requirement of the processing environment, and a wide range of applicable materials [1]. Meanwhile, ultraprecision processing of micro/nano structures can be realized by adopting an ultrafast laser [2,3].

During laser processing, irreversible damage will occur on the laser irradiated area due to the local high temperature and high pressure induced by ultrafast laser. As a wide-bandgap insulator/semiconductor, single-crystal diamond does not have enough free electrons in the conduction band before laser irradiation. When ultrafast laser interacts with single-crystal diamond, the material will first generate a large number of free electrons through nonlinear ionization mechanisms such as multiphoton ionization and avalanche ionization, which lead to a sharp increase in electron temperature. Subsequently, the hot electrons and plasma formed by the ionization of carbon atoms transfer energy to the lattice. With the release of energy, phase transformation, heat-affected zones, shock waves, and a series of damage behaviors such as lattice vacancies, dislocations, and cracks occur [4]. Zhao et al. [5] showed that the diamond was transformed into amorphous diamond with sp^3 bond after femtosecond laser processing. Girolami at el. [6] suggested that ultrafast laser can induce diamond to form graphite and the degree of graphite crystallinity depended on the laser fluence and scanning speed. Rehman et al. [7] observed an amorphous carbon layer mixed with sp^2 and sp^3 hybrid on the diamond surface after femtosecond laser processing, accompanied by a few cracks in a high laser fluence. Wang et al. [8] also observed cracks and chippings at the edge of microgrooves subjected to picosecond laser processing. Meanwhile, a kind of typical subwavelength periodic surface structure (so-called laser-

* Corresponding author.
E-mail address: zhangb@sustech.edu.cn (B. Zhang).

https://doi.org/10.1016/j.optlastec.2023.110120
Received 23 March 2023; Received in revised form 21 August 2023; Accepted 22 September 2023
Available online 28 September 2023

induced periodic surface structure: LIPSS) usually appears during laser processing. The variations in the LIPSS morphology under different process parameters were analyzed using single-point or single-path processing [9,10]. Despite a great variety of works focusing on surface processing features and the formation of damage, the effect of crystal orientation on ultrafast laser surface processing has rarely been studied. Diamond, a single-crystal material, has obvious anisotropy, which shows different optical and mechanical responses during laser processing and influences the final processed morphology. Thus, exploring the crystalline orientation effect on laser processing could provide insights for understanding the interaction between laser and material, and promote the application of ultrafast laser processing in manufacturing functional devices.

In this study, single-path scans were performed in the <100> and <110> directions on the (100) plane of single-crystal diamond to investigate the influence of crystalline orientation on laser processing. The evolution and formation mechanism of processing damage, including groove shape, cracks, chipping, phase transformation, and LIPSS were comprehensively analyzed. The crystalline orientation effect in the ultrafast laser surface processing of diamond was confirmed, and the mechanism was discussed based on the interaction process between the ultrafast laser and the material.

2. Experimental method

The equipment used for processing was an ultraviolet picosecond laser (Grace Laser, Blazer 40FUV) with a wavelength of 355 nm and a pulse width of $\tau < 15$ ps. A schematic of this process is shown in Fig. 1a. A Gaussian picosecond laser beam was guided into the scanning galvanometer and finally focused on the sample surface. The laser beam radius in the focal plane of the objective was $\omega_0 = 7.5\,\mu m$. The incident laser direction was perpendicular to the surface of the sample for single-path processing. To exclude the influence of the laser itself on the processing, the sample was rotated to make the <100> crystal direction or <110> crystal direction in the x-axis direction and the laser scribed on the surface of the sample along the x-axis. In the experiment, the scanning speed v varied from 0.5 to 9 mm/s, the laser fluences F varied from 0.566 to 1.56 J/cm^2, the number of scanning was once, and the repetition frequency f was fixed at 100 kHz. The laser fluence F was calculated from the equation $F = P/(\pi\omega_0{}^2 f)$, where P is the average output power.

The single-crystal diamond (Shenzhen Superhard Material Co., Ltd) used in this study was fabricated under high-pressure and high-temperature (HPHT) conditions. The dimensions of the bulk specimen were $3.0 \times 3.0 \times 1.0$ mm^3, and the surface roughness was approximately 1 nm after mechanical polishing. Electron backscatter diffraction (EBSD) was performed to distinguish the initial crystal orientation of the single-crystal diamond. Fig. 1b shows the EBSD inverse pole figure (IPF) map of the single-crystal diamond before laser processing. The IPF map indicates that the [100] crystal orientation of the single diamond is parallel to the normal direction (ND) of the specimen. Fig. 1c shows the corresponding relationship between the laser scanning directions in the atomic arrangement diagram of the (100) plane. The microstructure was characterized using scanning electron microscopy (SEM, FEI, Apreo 2S). Confocal laser scanning microscopy (Keyence, VK-X1000) was used to measure the cross-sectional profiles. The average profile of the groove was obtained by taking a total of 200 profiles at an interval of 0.2 μm from the acquired three-dimensional topography, and the dimensional information of the groove width and depth was measured. Raman spectra of the surface before and after laser processing were collected under ambient conditions using a confocal micro-Raman system (HORIBA, LabRAM HR Evolution) with a 532 nm laser excitation source. Focused ion beam (FIB, FEI, Helios 600i) was used to prepare subsurface samples. Before etching the subsurface, Pt and C layers were deposited on the surface of the grooves to protect the subsurface damage caused by laser ablation from being destroyed by the ion beam.

3. Experimental results

3.1. Evolution of groove shape

Fig. 2 and Fig. 3 show the variation of groove dimension along <100> and <110> directions with laser parameters. With an increase in the scanning speed, both the groove depth and width decrease. The equivalent number of pulses N for describing the deposition laser pulse per area can be calculated using the following equation [11]:

$$N = \frac{2\omega_0 f}{v} \tag{1}$$

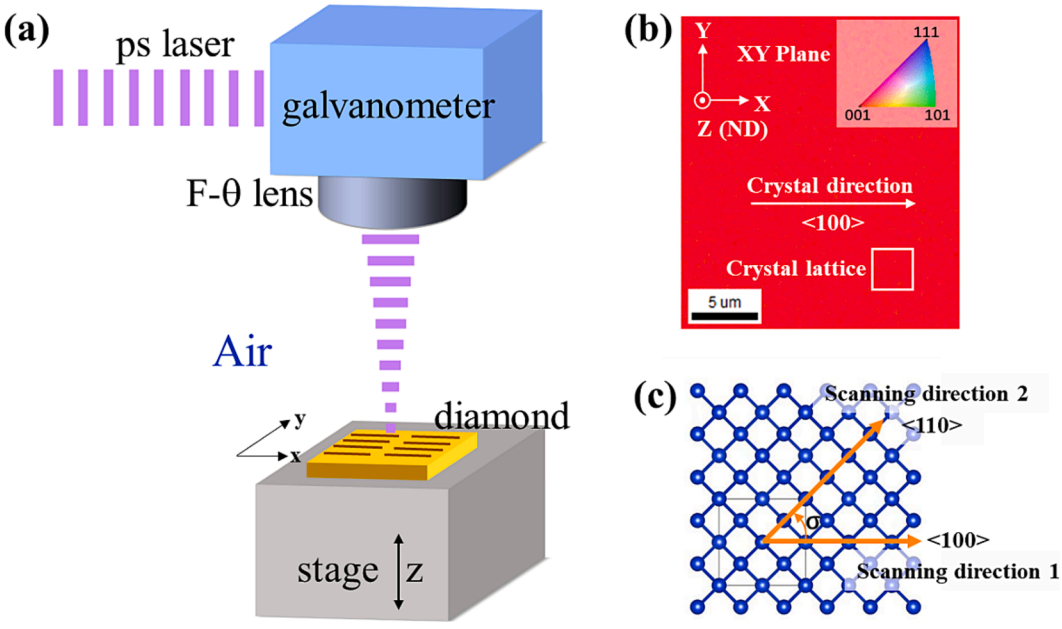

Fig. 1. (a) Processing schematic diagram. (b) EBSD IPF map of the sample, (ND: normal direction). (c) The relationship of laser scanning directions and the atomic arrangement diagram of (100) plane of the single-crystal diamond.

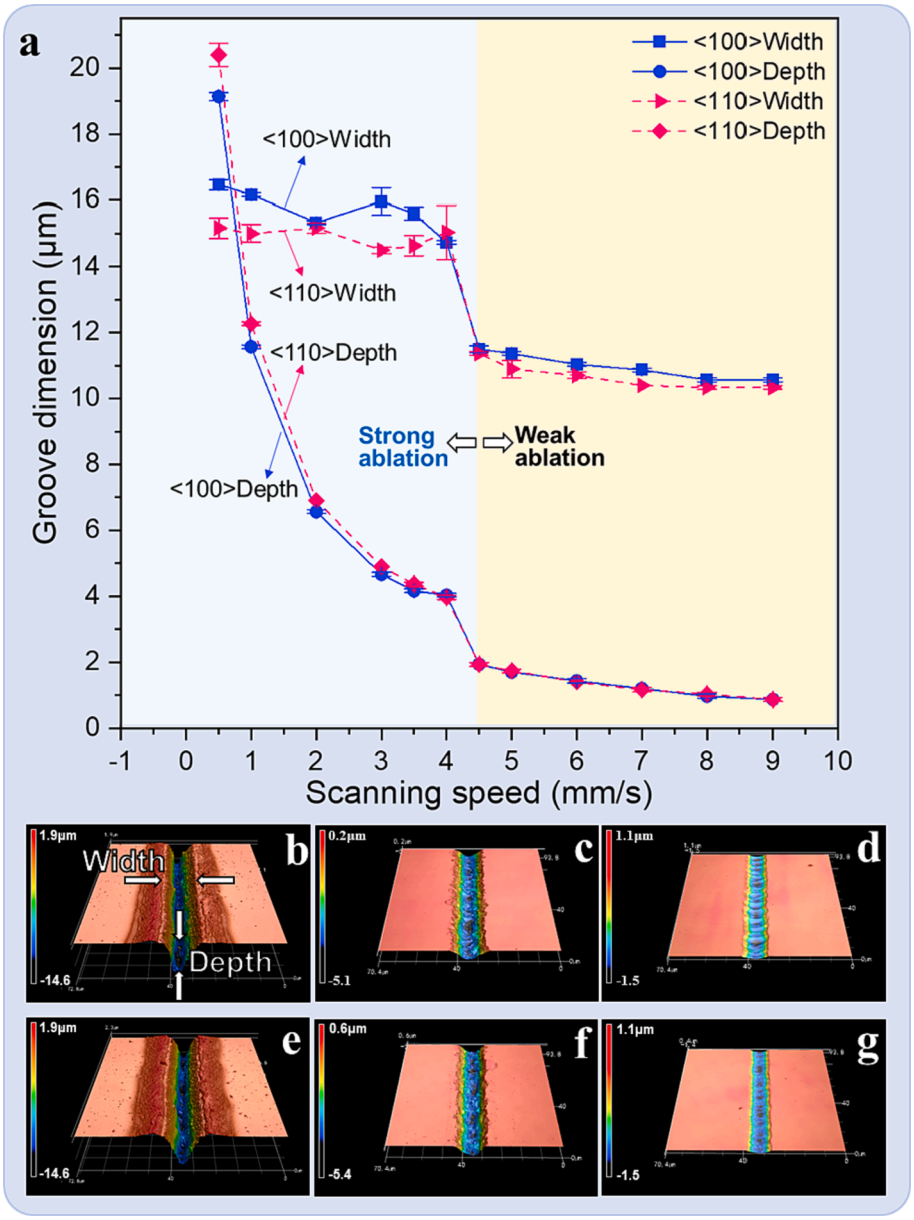

Fig. 2. Groove dimension along <100> and <110> directions. (a) Variation of groove dimension with scanning speed, laser fluence is 1.14 J/cm^2. (b-d) Three-dimensional images correspond to the grooves processed along <100> direction in (a), the scanning speed is 0.5, 3.5, and 7.0 mm/s, respectively. (e-g) Three-dimensional images correspond to the grooves processed along <110> direction in (a), the scanning speed is 0.5, 3.5, 4.5, and 7.0 mm/s, respectively.

Under a certain laser repetition frequency *f*, increasing the scanning speed is equivalent to decreasing the pulse number irradiated per spot. When the laser fluence is fixed, the laser energy received on the material decreases with an increase in the scanning speed, and the removal rate of the material decreases. Therefore, both the groove width and depth decrease with an increase in scanning speed. From Fig. 2a, it can be observed that the scanning speed of 4.5 mm/s (with a pulse number of 333) represents a turning point for the groove size, after which the groove size decreases slowly. Additionally, this scanning speed marks a transition point in the ablation state. Combined with the three-dimensional images in Fig. 2b-g, it can be seen that the cross-section profile gradually changes from the initial deep V-shape to a shallow U-shape as the scanning speed increases. However, the ablation profiles differ when processing along different crystal directions. As shown in Fig. 3, processing along the <110> direction tends to create larger depth-to-width ratios compared to the <100> direction.

3.2. Surface morphology

The typical surface morphologies of the ablated groove along different directions also show differences (Fig. 4). To better relate the deposited laser energy to the processing phenomenon, the pulse number is used instead of the scanning speed in the description below. When the pulse number is less than 333, as shown in Fig. 4a and 4d, the surfaces of the grooves have no collateral damage, such as cracks and chippings, but present a clear LIPSS structure, demonstrating that the grooves are in a weak ablation state. When the pulse number is higher than 333, as shown in Fig. 4b, c and e, f, the grooves along both directions present a large ablative depth, microcracks, and chippings, indicating that they are in a strong ablation state [12,13].

In the pulse number range of 375–750, serious chipping and cracks appear in the groove, and the typical surface morphologies are shown in Fig. 4b and 4e. Significant differences in the characteristics of the chippings and cracks can be observed. These differences are less affected

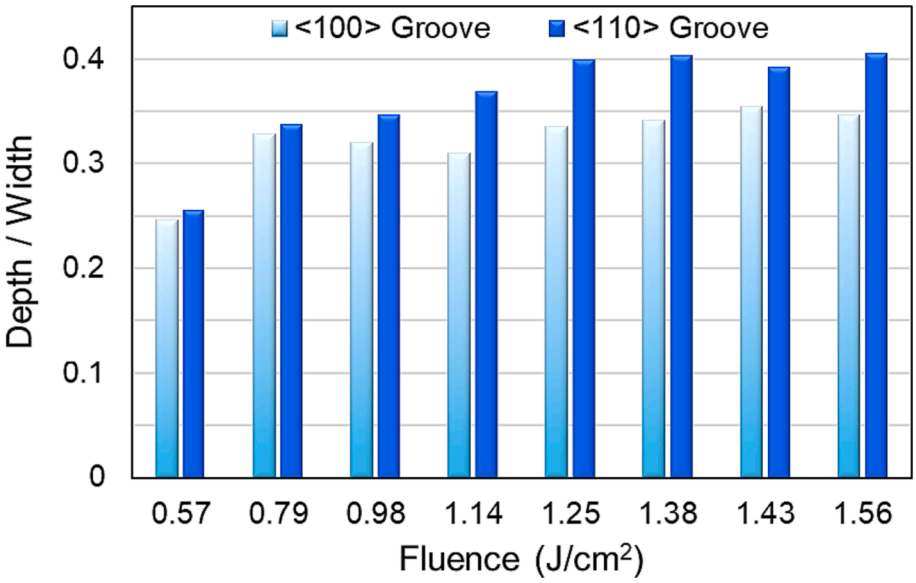

Fig. 3. Variation of the ratio of groove depth to width with laser fluence, scanning speed is 3 mm/s.

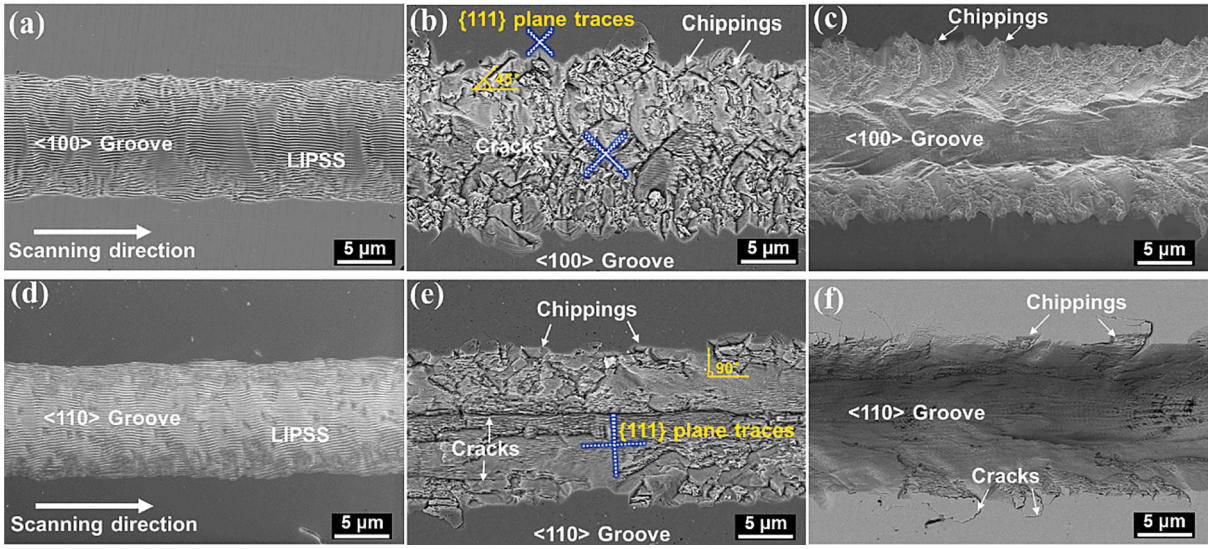

Fig. 4. SEM images of the grooves along different directions: (a-c) <100> direction, pulse number is 300, 500, and 1500, respectively. (d-f) <110> direction, pulse number is 250, 500, and 1500, respectively. All laser fluences are 1.14 J/cm^2, and {111} plane traces were obtained from EBSD IPF analysis.

by the pulse number and laser fluence and mainly depended on the crystal direction of the laser scanning. The edge chipping of the groove processed along the <100> direction presents a sawtooth-like shape, and the cracks in the groove are cross-distributed. The angle between the crack direction and the processing direction is approximately 45°. Compared with the <100> direction, the <110> edge chipping is relatively regular, and the material crack along or perpendicular to the scanning direction, forming rectangular shape chippings. A crystallographic analysis was conducted using EBSD to investigate the main crack paths after processing. As displayed in Fig. 4b and 4e, the crystallographic equivalent traces of the {111} planes of diamond with a face-centered cubic (FCC) structure are marked by blue dotted lines. Trace analysis demonstrates that the majority of the cracks are parallel to the traces of the {111} planes. The ratio of fracture energy of diamond {100}, {110}, {111} planes is about 7:2.8:1, which indicates that the {111} plane of diamond has the lowest strength and requires the lowest fracture energy [14]. When laser-induced stress is applied, fracture occurs preferentially on the {111} cleavage plane. In the pulse number range of 1500–3000, as shown in Fig. 4c and f, improvements are observed in chipping and cracking, and smooth groove bottoms are formed. This phenomenon is consistent with the experimental observations by Wang et al. [8] when increasing the laser fluence. It is worth noting that the grooves along <110> exhibit more regular edges and flatter sidewalls than the <100> ones. Interestingly, Wen et al. [15] also found that microgrooves along <110> showed better inner surface morphology compared to those along <100> when using nanosecond laser to process diamond, due to reduced attachment of graphite particles on the <110> sidewalls.

3.3. Phase transformation

After processing, Raman spectroscopy measurements were performed at the center of the grooves processed in two crystal directions. As shown in Fig. 5, when the pulse number is less than 429, there is only one diamond peak in the Raman spectrum located around 1331 cm^{-1}, corresponding to the sp^3 phase. When the pulse number is higher than

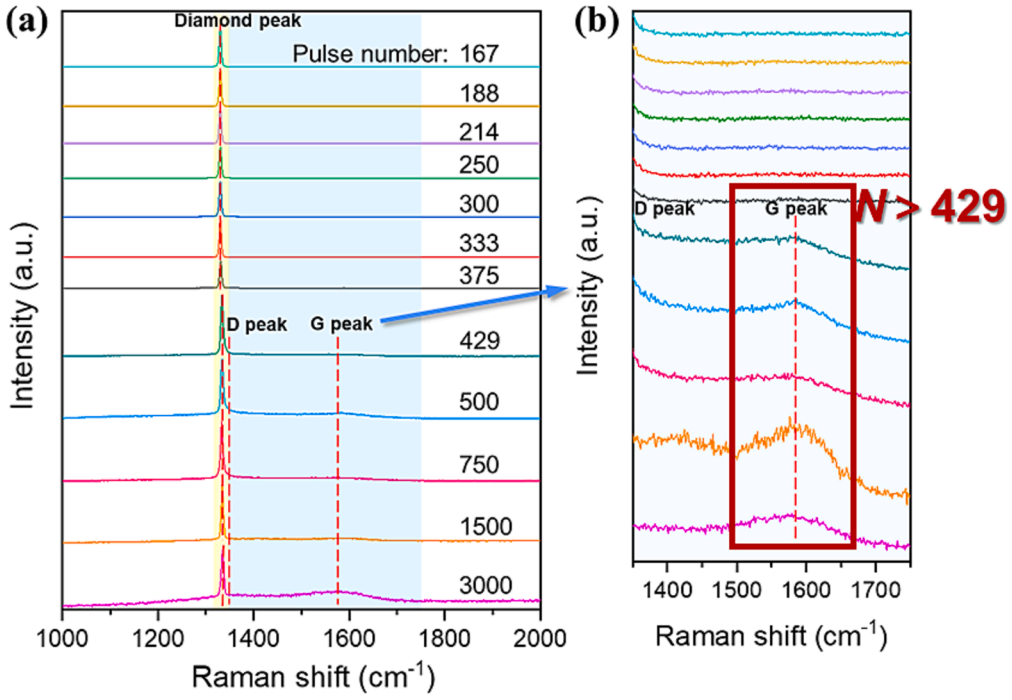

Fig. 5. (a) Raman spectra of the grooves along the <100> direction at different pulse numbers, all fluences are fixed as 1.14 J/cm^2. (b) enlarged view of the spectra at 1350–1750 cm^{-1} in (a).

429, a wide band appears in the Raman spectrum of the sample processed along the <100> direction. The wide band is composed of smeared and merged peaks of the D peak at approximately 1,350 cm^{-1} and the G peak at approximately 1,580 cm^{-1}. As reported in previous studies, the D peak is caused by the irregular lattice vibration mode of amorphous, which is associated with the lattice defects of C atoms. The G peak is formed by the in-plane bond-stretching motion of ordered graphite sp^2 C atoms [16,17]. Therefore, the evolution of the Raman spectra indicates that graphitization initiates when the pulse number exceeds 429 and along the <100> direction. At high pulse numbers, the sp^3 phase of diamond partially transforms into the amorphous and graphite phases. Fig. 6 shows the Raman spectra of the grooves processed along the <110> direction at different pulse numbers. When the pulse number is higher than 333, a wide band composed of D and G peaks exists. By comparing Fig. 5 and Fig. 6, it can be observed that the graphitization initiates easier along the <110> direction under the same processing conditions.

To further analyze the crystalline orientation effect in phase

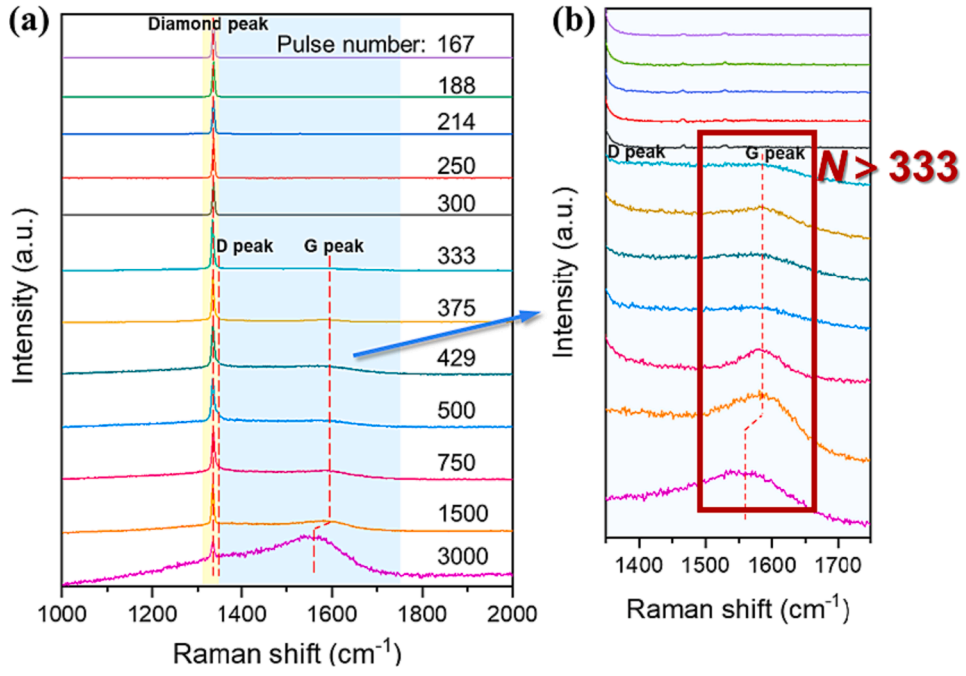

Fig. 6. (a) Raman spectra of the grooves along the <110> direction at different pulse numbers, all fluences are fixed as 1.14 J/cm^2. (b) enlarged view of the spectra at 1350–1750 cm^{-1} in (a).

transformation, the samples processed at a high pulse number of 3000 were observed by SEM to compare the deposition. Fig. 7a and 8a present overviews of the unilateral deposition layer processed along the <100> and <110> directions, respectively. The Raman spectra of the regions marked by dashed circles at the same distance from the spot center are shown in Fig. 7b and 8b. It can be observed that a diamond peak and an obvious G band, demonstrate that the depositions are composed of sp^3 phase and sp^2 graphite phases. The content relationship between the diamond and graphite phases can be evaluated by comparing the peak intensity ratio of the diamond peak (I_{Dia}) and G band (I_G) [18]. In the <100> direction, the ratio of I_{Dia} / I_G is approximately 1.3 and the ratio is approximately 1.1 when processing along the <110> direction. This indicates that the depositions processed along the <110> direction have a higher sp^2 phase content. In addition, the measurement of the deposition profile shows that under the same processing conditions, the deposition layer induced by laser scanning along the <110> direction is wider, 9.99 μm along the <100> direction and 11.27 μm along the <110> direction.

Fig. 7c–f and Fig. 8c–f show the detailed morphology of the debris. There is no significant difference in the morphology of the debris processed along the <100> or <110> direction. Both can be divided into four regions based on the distance from the center of the laser spot. The debris near the groove shows a rippled morphology (Fig. 7c and Fig. 8c). In the outer area (Fig. 7d and Fig. 8d), debris condenses into large cauliflower-like depositions of different sizes, and in the outer area (Fig. 7e and Fig. 8e), the deposits show the characteristics of uniform small round particles. The deposits farther from the spot center appear as a thin layer of fine particles (Fig. 7f and Fig. 8f). The further away from the spot center, the smaller the debris particle size.

3.4. Subsurface damage

The subsurface damage caused by processing greatly affects the mechanical and fatigue properties of the material [19]. To facilitate the analysis of the subsurface damage forms after ultrafast laser processing, groove cross-sections with severe surface cracks processed at *N* 500, 1.25 J/cm^2 were prepared by FIB. Fig. 9 shows the representative cross-sectional images beneath the groove processed along the <100> and <110> directions. The cross-sections processed along both crystal directions have damaged forms of cracks and voids. The cracks propagate from the groove surface to the subsurface, mostly from the tip of the sawtooth cross-sectional profile. Voids mainly exist near the surface. The main driving force for void formation is the relaxation of the compressive stress generated under the photomechanical effect. The evolution of voids and cracks leads to the fragmentation and the ejection of large chunks of the material [20]. Comparing the subsurface damage along different directions in Fig. 9, no cracks are observed at the bottom of the groove processed along the <100> direction in the cross-sectional image (Fig. 9b), but cracks are observed on the side (Fig. 9c). However, cracks are extending down 1.0 μm at the bottom of the groove processed along the <110> direction (Fig. 9e), and a large number of cracks also appear on the side (Fig. 9f).

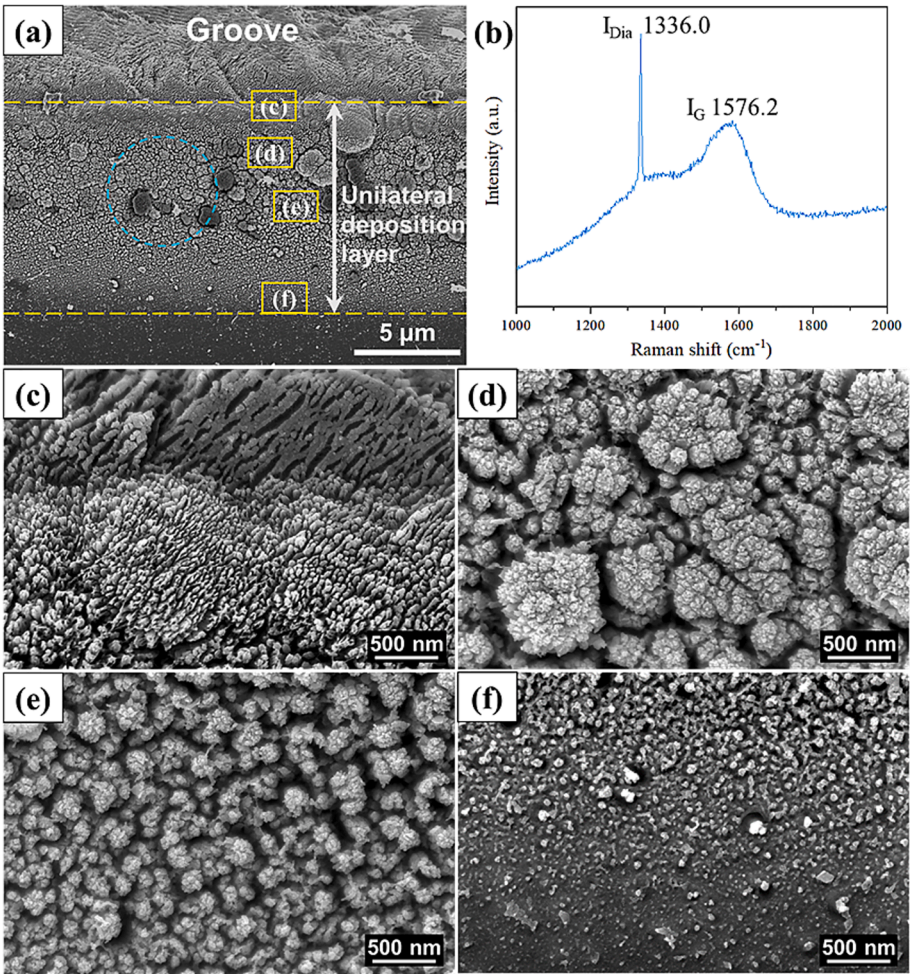

Fig. 7. SEM images of debris produced along <100> direction, pulse number is 3000, (a) overview of unilateral deposition layer of the groove, the width of the deposition layer is marked in dotted lines. (b) Raman spectrum of the dashed circle region in (a), (c) rippled debris, (d) large debris particles, (e) small round particles, (f) thin layer particles.

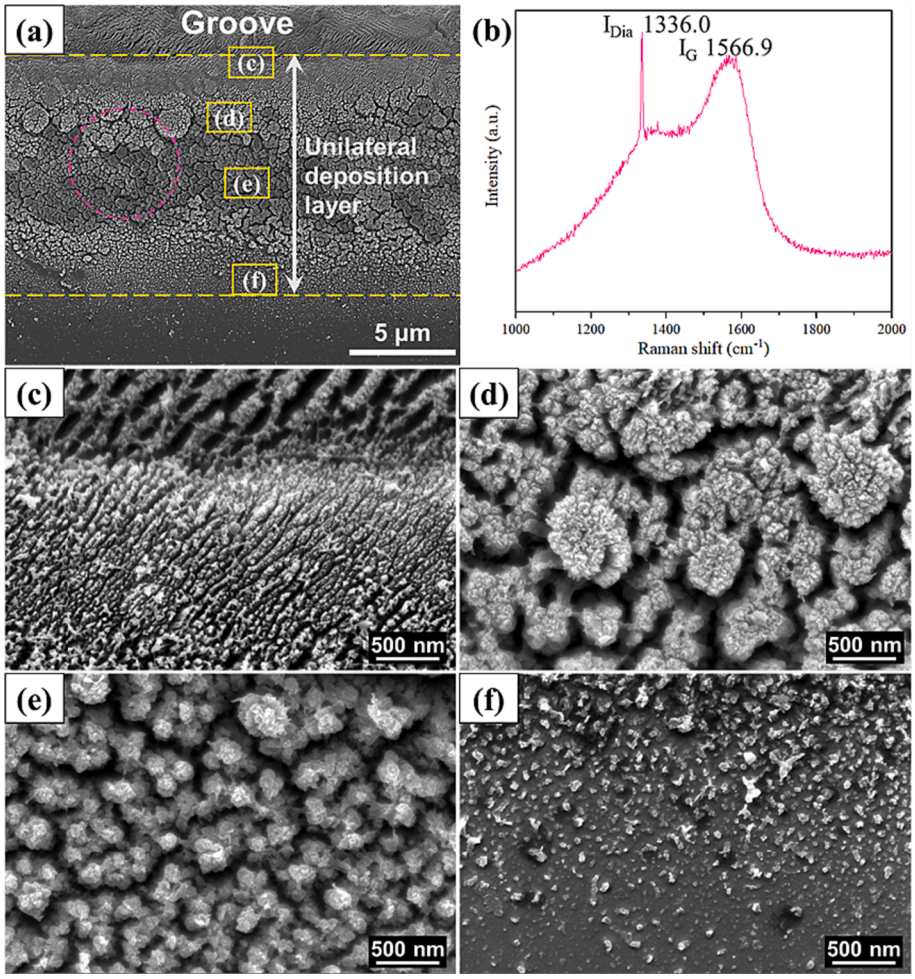

Fig. 8. SEM images of debris produced along <1 1 0> direction, pulse number is 3000, (a) overview of unilateral deposition layer of the groove, the width of the deposition is marked in dotted lines. (b) Raman spectrum of the dashed circle region in (a), (c) rippled debris, (d) large debris particles, (e) small round particles, (f) thin layer particles.

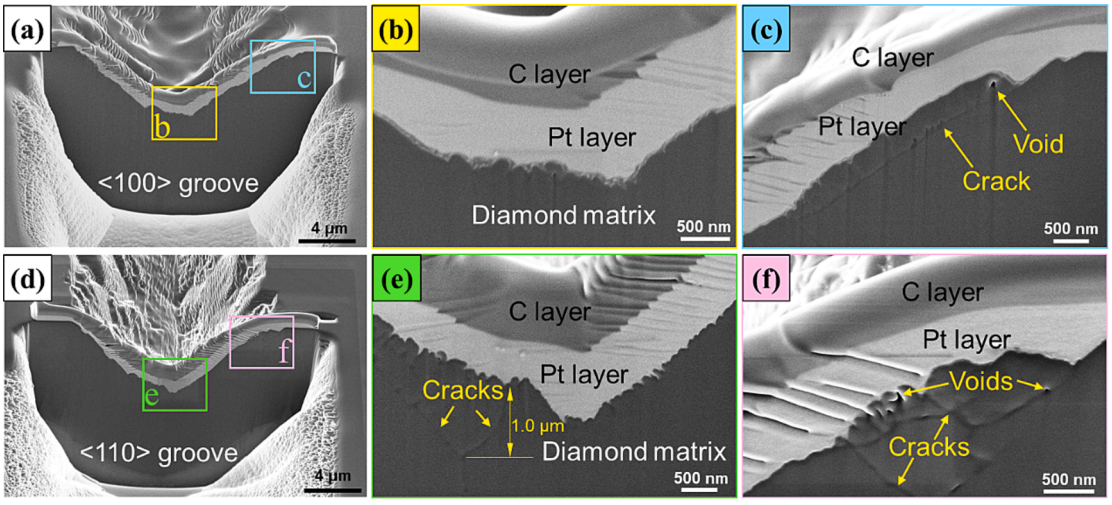

Fig. 9. Representative cross-sectional images beneath the groove surface. (a-c) The groove subsurface along <1 0 0> direction, where (b) and (c) are enlarged views of local areas of (a); (d-f) the groove subsurface along <1 1 0> direction, where (e) and (f) are enlarged views of local areas of (d). Grooves were processed at *N* 500, 1.25 J/cm^2.

3.5. Characteristics of LIPSS

Laser-induced periodic surface structures (also known as surface ripples or nanogratings) are often accompanied by ultrafast laser processing with a laser fluence close to the material threshold [21–23]. Regarding its formation mechanism, one widely recognized theory

states that LIPSS is created by the periodic energy distribution from the interference between the incident laser and laser-excited surface plasmon polaritons (SPPs) [24]. Meanwhile, LIPSS can be divided into LSFL (low spatial frequency LIPSS, $\lambda/2 < \Lambda < \lambda$) and HSFL (high spatial frequency LIPSS, $\Lambda < \lambda/2$) according to the relationship between the spatial period (Λ) and the incident laser wavelength λ [25].

Fig. 10 shows the evolution of the LIPSS morphology at the bottom of the grooves with increasing pulse number and along the <100> direction. When the pulse number is 214 and 300, regular LSFL is observed on the surface (Fig. 10a and 10b), with a period of approximately 272 and 257 nm, respectively. However, as the pulse number increases to 375, a significant number of cracks are distributed on the {111} cleavage planes within the groove, and the LIPSS become disordered (Fig. 10c). Fig. 10d shows an HSFL with a period of approximately 100 nm at 1500 pulses. The overall period shows a decreasing trend with an increase in pulse number. The LIPSS characteristics within the grooves processed along the <110> direction are depicted in Fig. 11. Notably, the LIPSS produced along the <110> direction exhibit a higher degree of disorder. Compared to Fig. 10, the LIPSS along the <110> direction has a similar period size to the <100> direction in a weak ablation state, but the integrity of the LIPSS is worse along the <110> direction and is accompanied by fragmentation (Fig. 11a and b). In addition, the LIPSS morphologies are quite different in strong ablation state, as shown in Fig. 10c and Fig. 11c, when a large number of cracks distributed along the {111} planes appear in the groove (detailed analysis is discussed in Section 4).

4. Discussion

4.1. Formation mechanism of processing damage

There are some commonalities in the formation of processing damage along the different crystal directions. As the scanning speed v decreases, the pulse number increases. According to the incubation model of plasma [26,27], the relationship between the N-pulse damage threshold F_{th} (N) and the single-pulse damage threshold F_{th} (1) can be expressed as follows:

$$F_{th}(N) = F_{th}(1)N^{S-1} \tag{2}$$

where S is an incubation coefficient less than 1. This suggests that the damage threshold should decrease with an increase in the pulse number, and the utilization rate of laser energy is higher at this time, resulting in a higher material removal rate. The pulse number 333 ($v = 4.5$ mm/s) in Fig. 2 is the turning point of the groove depth and ablation state owing to the incubation effect occurring. When the pulse number is higher than 333 ($v < 4.5$ mm/s). The incubation effect under multiple pulses is due to the formation of a large number of cracks and micro/nano structures in the groove, which increase the laser absorption rate of the material [28]. In this strong ablation state, a deeper V-shaped groove is formed on the surface. According to the theoretical model of interference between SPPs and the incident laser, the spatial period Λ of LIPSS can be expressed as follows [29,30]:

$$\Lambda = \frac{\lambda}{1 \pm sin\theta} \tag{3}$$

where θ is the angle of incidence measured from the surface normal. When the pulse number increase, the laser is incident on the sidewall at an increasing angle, and multiple scattering and interference with SPPs occur in the groove, resulting in the formation of LIPSS with a reduced period, which is consistent with previous reports [10,31].

As the pulse number increases, the superposition of the pulse energy leads to heat accumulation. The temperature diffusion time is approximately 10^{-12} s [32], which is close to the pulse width of the laser; therefore, it is difficult for materials to transfer heat to the surrounding unirradiated area. The surface temperature of the material exceeds the graphitization temperature of the diamond in air, $T > T_g \approx 700$ °C [33], and the diamond undergoes graphitization phase transformation. The local high-temperature and high-pressure environment also leads to an amorphous phase [5]. Thermal stress relaxation dominates cracks and chipping formation [34].

Further understanding of crack generation conditions helps to control cracking formation in combination with laser processing parameters. Bloembergen [35] showed that laser energy absorption begins from near-surface defects in diamond such as cracks, pores, and impurities, causing a localized temperature increase. The difference ΔT between the initial and maximum temperatures, caused by laser irradiation, results in a high triaxial stress σ. The theoretical model of fracture mechanics under thermal stress proposed by Hasselman [36] is used here to describe the initiation and propagation behavior of cracks in ultrafast laser processing single-crystal diamond:

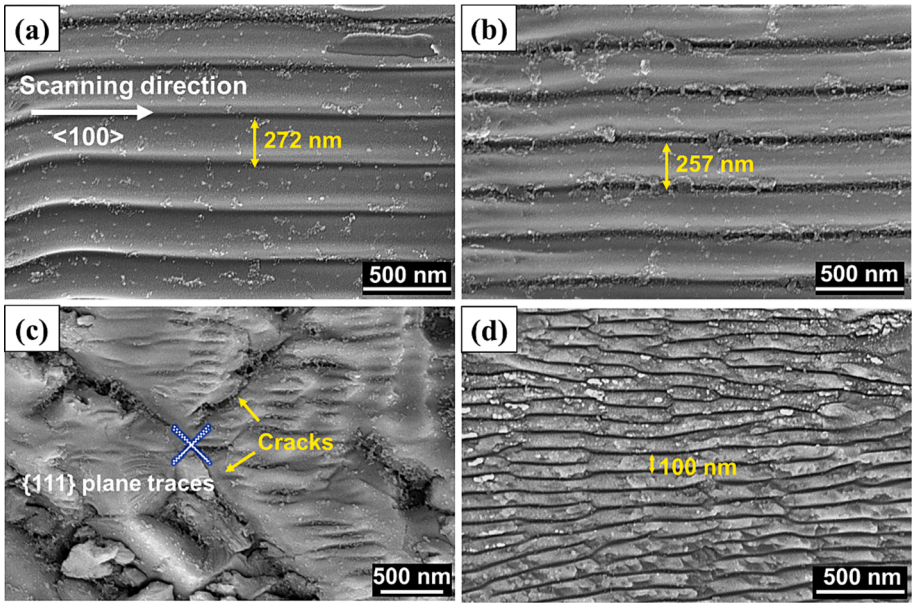

Fig. 10. The evolution of LIPSS along <100> direction with pulse number, (a-d) The pulse number is 214, 300, 375, and 1500, respectively, and laser fluence is 1.14 J/cm^2.

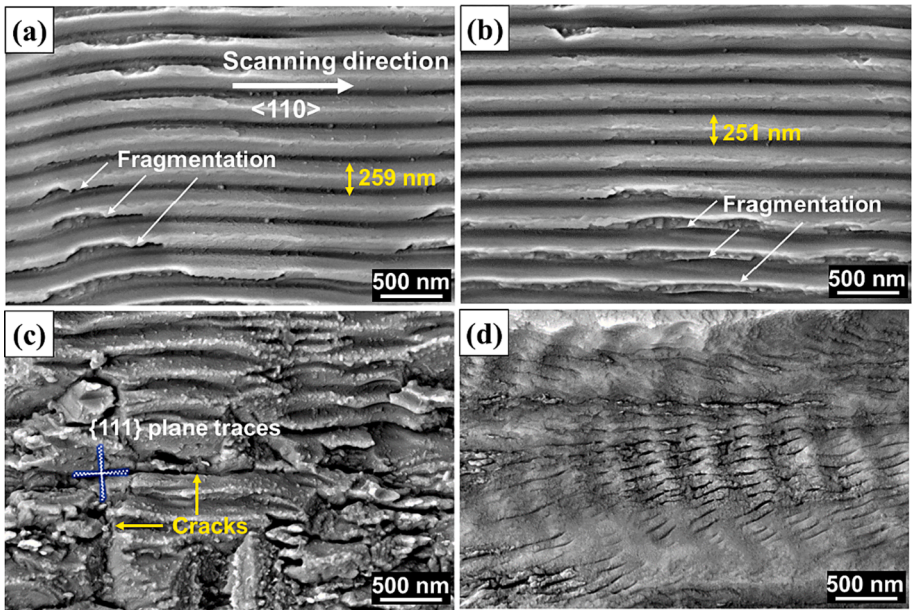

Fig. 11. The evolution of LIPSS along <1 1 0> direction with pulse number, (a-d) The pulse number is 214, 300, 375, and 1500, respectively, and laser fluence is 1.14 J/cm^2.

$$\sigma = \frac{\alpha E \Delta T}{1 - 2\upsilon} \tag{4}$$

where α is the coefficient of thermal expansion; E is Young's modulus of elasticity; and υ is Poisson's ratio. Because the laser energy is Gaussian, ΔT and σ depend on the distance from the spot center. The total energy (W_t) per unit volume is the sum of the elastic and fracture energies of the cracks, which can be described by the following equation [36]:

$$W_t = \frac{3(\alpha\Delta T)^2 E_0}{2(1-2\upsilon)}\left[1 + \frac{16(1-\upsilon^2)Ml^3}{9(1-2\upsilon)}\right] + 2\pi Ml^2 G \tag{5}$$

where E_0 is Young's modulus of the crack-free material, l is the crack length, M is the number of cracks per unit volume, and G is the surface fracture energy. Based on the condition of the crack instability,

$$\frac{dW_t}{dl} = 0 \tag{6}$$

the critical temperature difference ΔT_c of the crack instability can be calculated. Consequently, crack length does not change in the range $0 < \Delta T < \Delta T_c$. At $\Delta T = \Delta T_c$, the crack propagates in a kinetic behavior. It can be concluded that by controlling the ΔT on the surface of the material caused by laser irradiation, the cracking can be inhibited.

4.2. Damage evolution and crystalline orientation effects

The experimental results show that both crystal orientation and laser parameters strongly influence damage characteristics during ultrafast laser processing. Based on the above results, the evolution of damage in ultrafast laser processing single-crystal diamond can be divided into three stages according to the pulse number, as shown in Fig. 12a and b.

a) $N \sim$ 166–333 ($v \sim$ 9–4.5 mm/s), weak ablation stage

When the pulse number is 166–333, the interval between pulses is large, and the thermal accumulation effect is not obvious. The resulting temperature difference ΔT does not exceed the critical temperature difference ΔT_c for crack propagation under thermal stress. Therefore, no cracks are observed on the surface and edge of the grooves. At this stage, surface graphitization is initiated easier along the <1 1 0> direction as the pulse number increases. The material is removed via vaporization, leaving shallow grooves.

b) $N \sim$ 375–750 ($v \sim$ 4–2 mm/s), severe cracking stage

As the pulse number increases to 375–750, the temperature difference ΔT generated by the superposition of pulse energy exceeds the critical temperature difference ΔT_c for crack propagation under thermal stress, and the cracks expand rapidly. The fragmented materials are removed under the impact of the plasma and then fall in and around the groove. Because the depth of the ablation layer is less than the cracking depth, severe cracks and chipping along the {1 1 1} cleavage planes remain on the processed surface. Since the angle between the processing crystal direction and the {1 1 1} plane is different, the crack distribution of the groove is also different. At this stage, the degree of surface graphitization is further intensified under the thermal accumulation effect. The material is accompanied by subsurface damage, such as cracks and voids. The material removal method at this stage involves vaporization and fragmentation.

c) $N \sim$ 1,500–3,000 ($v \sim$ 1–0.5 mm/s), severe phase transformation stage

When the pulse number is further increased to 1,500–3,000 ($v \sim$ 1–0.5 mm/s), the resulting temperature difference ΔT also exceeds the critical temperature difference ΔT_c. Due to the Gaussian energy distribution of the spot, the ablation depth in the center of the groove is higher than the cracking depth, and the cracking layer can be completely removed to form a smooth bottom of the groove; however, there is still slight chipping in the edge area of the spot radiation. Graphitization is severe at this stage. Upon further increasing the pulse number, a large amount of carbon vapor condenses to form deposited layers on both sides of the groove.

Based on the above results and analysis, we propose a phase transformation-driven damage anisotropy mechanism (as shown in Fig. 12), that is, the difference in phase transformation induced by ultrafast laser processing along different crystal orientations affects the distribution and absorption of laser energy, resulting in different processing characteristics. For single-crystal diamond with a cubic lattice, when laser scanning along the <1 0 0> and <1 1 0> crystal directions, the crystal plane for energy deposition is the {1 0 0} and {1 1 0} plane, respectively (as shown in Fig. 12c). On the one hand, the cleavage energy of {1 0 0} plane is about 2.5 times larger than that of {1 1 0} surfaces; on the other hand, the transformation of diamond {1 0 0} plane to graphite plane requires much more complex atomic rearrangement than that of the {1 1 0} plane composed of sixfold rings, as shown in Fig. 12d.

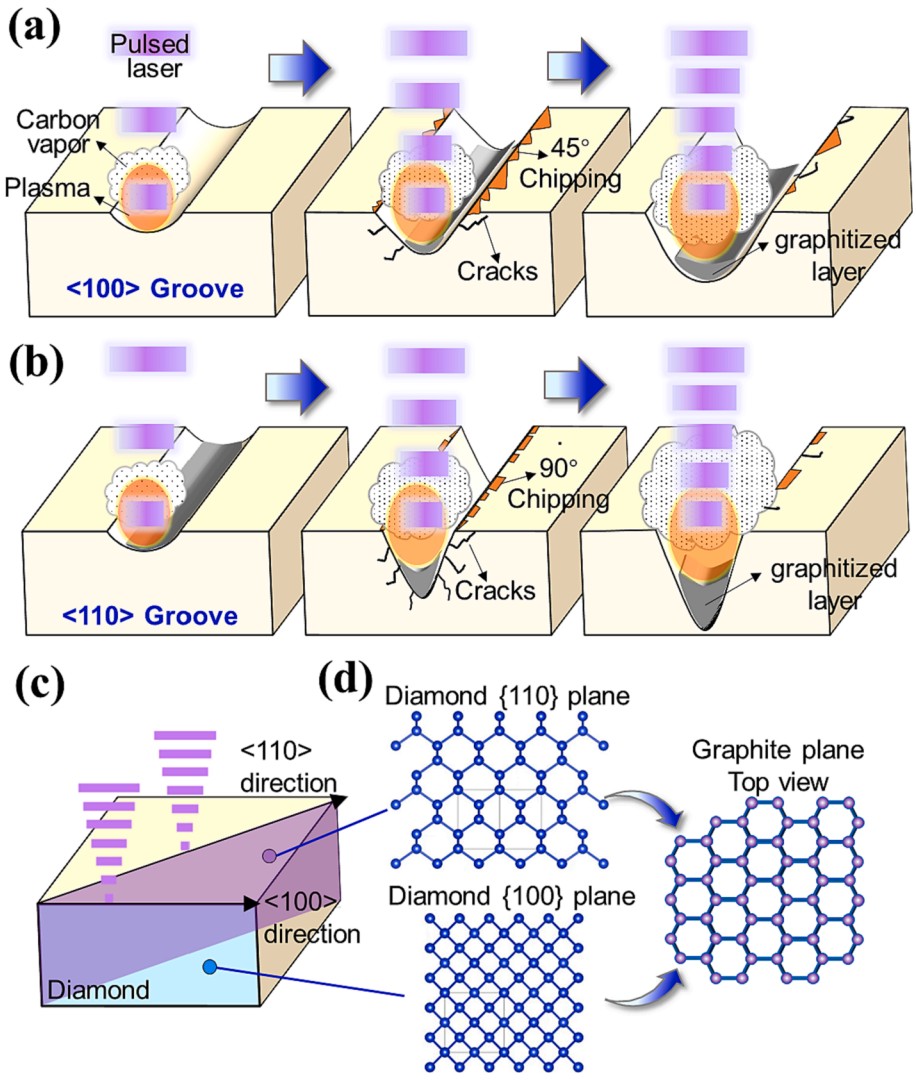

Fig. 12. Schematic diagram of damage evolution with increasing pulse number (a) <100> direction, (b) <110> direction, (c-d) phase transformation-driven damage anisotropy mechanism, and top views of diamond {110},{100} planes and {0001} graphite planes.

As a result, the former requires overcoming a substantially higher energy barrier to form graphite-like structure [37]. Therefore, in the first stage (weak ablation stage) under the irradiation of a small number of pulses, graphitization initiated easier along the <110> direction. Compared with diamond, the graphite phase significantly enhances the absorption of laser energy [38] and transfers part of the energy to the diamond lattice. This resulted in higher thermal stress and more severe subsurface damage along the <110> direction in the second stage with moderate pulse numbers. As the pulse number increases, graphite and diamond phase vaporization under heat accumulation, and a large amount of carbon vapor condenses to form a wider deposition layer. This is also the reason for a higher depth-to-width ratio of the grooves processed along the <110> direction. Differences in phase transformation, groove shape, and defects (e. g. cracks) can affect the absorption of laser energy, thereby affecting the behavior of SPPs and leading to significant differences in the morphology of LIPSS. In addition, some scholars believe that for wide-bandgap crystals, the nonlinear ionization rate of ultrafast lasers interacting with materials is related to the crystal orientation, which also leads to the orientation effect of LIPSS [39,40].

5. Conclusions

In this work, the damage evolution and crystalline orientation effects in ultrafast laser micro/nano processing of single-crystal diamond are investigated by considering the groove shape, surface morphology, graphitization, subsurface damage, and LIPSS. The major conclusions are summarized as follows:

(1) As the pulse number increase, the picosecond laser processing of the diamond changes from weak to strong ablation, and the accompanying incubation effect caused the groove size to increase significantly. Simultaneously, heat accumulation leads to graphitization. Thermal stress relaxation dominates cracks and chipping formation, and the cracks are mainly distributed along the {111} planes.

(2) Both crystal orientation and laser parameters strongly influence damage characteristics during ultrafast laser processing. The evolution of damage can be divided into three different stages, named weak ablation stage, severe cracking stage, and severe phase transformation stage. Since the angle between the processing crystal direction and the {111} plane is different, the crack distribution of the groove is also different, forming 45° chipping along the <100> direction and 90° chipping along the <110> direction. The Raman results indicate a greater degree of graphitization observed along the <110> direction.

(3) For single-crystal diamond with a cubic lattice, a new mechanism

of phase transformation-driven damage anisotropy is proposed considering the cleavage energy and atomic rearrangement energy of laser energy deposited crystal planes. That is, when laser is applied to different crystal directions, the energy barriers that need to be overcome for phase transformation are different, leading to a preferential phase transformation in a certain direction, which makes the absorption rate of laser energy locally enhanced, and finally leads to different processing characteristics.

This study provides a new perspective on the interaction process between ultrafast laser and single-crystal diamond, and inspires us to make full use of material properties to regulate laser-induced damage, which is crucial for high-precision, low-damage micro/nano processing.

Declaration of Competing Interest

The authors declare that they have no known competing financial interests or personal relationships that could have appeared to influence the work reported in this paper.

Data availability

Data will be made available on request.

Acknowledgments

This study was financially supported by the Shenzhen Science and Technology Innovation Commission (Grant No. GJHZ20210705141807023, KQTD20190929172505711, JSGG20210420091802007, JCYJ20210324115413036). The authors thank Prof. Shuai Wang and Prof. Shaolin Xu for valuable discussions regarding the experimental and analytical results of this study. Raman data were obtained using equipment maintained by the Southern University of Science and Technology Core Research Facilities. Finally, special thanks to the Ultrafast Laser Micro-/Nanofabrication Lab of SUSTech for providing the laser equipment support for this study.

References

[1] B. Ali, I.V. Litvinyuk, M. Rybachuk, Femtosecond laser micromachining of diamond: Current research status, applications and challenges, Carbon 179 (2021) 209–226.
[2] J. Cheng, C.S. Liu, S. Shang, D. Liu, W. Perrie, G. Dearden, K. Watkins, A review of ultrafast laser materials micromachining, Opt. Laser Technol. 46 (2013) 88–102.
[3] Y. Guo, P. Qiu, S.L. Xu, G.J. Cheng, Laser-induced microjet-assisted ablation for high-quality microfabrication, Int. J. Extrem. Manuf. 4 (2022).
[4] D.Z. Tan, K.N. Sharafudeen, Y.Z. Yue, J.R. Qiu, Femtosecond laser induced phenomena in transparent solid materials: Fundamentals and applications, Prog. Mater. Sci. 76 (2016) 154–228.
[5] J.G. Zhao, C. Zhang, F. Liu, G.J. Cheng, Understanding femtosecond laser internal scribing of diamond by atomic simulation: Phase transition, structure and property, Carbon 175 (2021) 352–363.
[6] M. Girolami, A. Bellucci, P. Calvani, S. Orlando, V. Valentini, D.M. Trucchi, Raman investigation of femtosecond laser-induced graphitic columns in single-crystal diamond, Appl. Phys. A-mater. 117 (2014) 143–147.
[7] Z.U. Rehman, K.A. Janulewicz, Structural transformation of monocrystalline diamond driven by ultrashort laser pulses, Diam. Relat. Mater. 70 (2016) 194–200.
[8] H.L. Wang, Q.L. Wen, X.P. Xu, J. Lu, F. Jiang, C.C. Cui, Ablation characteristics and material removal mechanisms of a single-crystal diamond processed by nanosecond or picosecond lasers, Opt. Express 29 (2021) 22714–22731.
[9] E.M. Hsu, N.A. Mailman, G.A. Botton, H.K. Haugen, Microscopic investigation of single-crystal diamond following ultrafast laser irradiation, Appl. Phys. A-mater. 103 (2011) 185–192.
[10] E. Granados, M. Martinez-Calderon, M. Gomez, A. Rodriguez, S.M. Olaizola, Photonic structures in diamond based on femtosecond UV laser induced periodic surface structuring (LIPSS), Opt. Express 25 (2017) 15330–15335.
[11] H.W. Choi, S. Bong, D.F. Farson, C.M. Lu, L.J. Lee, Femtosecond laser micromachining and application of hot embossing molds for microfluid device fabrication, J. Laser Appl. 21 (2009) 196–204.
[12] P.R. Herman, R.S. Marjoribanks, A. Oettl, K. Chen, I. Konovalov, S. Ness, Laser shaping of photonic materials: deep-ultraviolet and ultrafast lasers, Appl. Surf. Sci. 154 (2000) 577–586.
[13] P.R. Herman A. Oettl K.P. Chen R.S. Marjoribanks Laser micromachining of 'transparent' fused silica with 1-ps pulses and pulse trains Conference on Commercial and Biomedical Applications of Ultrafast Lasers 1999 San Jose, Ca 148 155.
[14] R.H. Telling, C.J. Pickard, M.C. Payne, J.E. Field, Theoretical strength and cleavage of diamond, Phys. Rev. Lett. 84 (2000) 5160–5163.
[15] Q.L. Wen, X.Y. Wei, X.P. Xu, J. Lu, C.C. Cui, Study on ultraviolet laser processing of a single-crystal diamond along (100) and (110) crystal orientations, Opt. Laser Technol. 149 (2022).
[16] A.C. Ferrari, J. Robertson, Interpretation of Raman spectra of disordered and amorphous carbon, Phys. Rev. B 61 (2000) 14095–14107.
[17] T. Guillemet, Z.Q. Xie, Y.S. Zhou, J.B. Park, A. Veillere, W. Xiong, J.M. Heintz, J. F. Silvain, N. Chandra, Y.F. Lu, Stress and phase purity analyses of diamond films deposited through laser-assisted combustion synthesis, Acs. Appl. Mater. Inter. 3 (2011) 4120–4125.
[18] B. Paramanik, D. Das, Synthesis of nanocrystalline diamond embedded diamond-like carbon films on untreated glass substrates at low temperature using (C2H2 + H-2) gas composition in microwave plasma CVD, Appl. Surf. Sci. 579 (2022).
[19] B. Zhang, J.F. Yin, The 'skin effect' of subsurface damage distribution in materials subjected to high-speed machining, Int. J. Extrem. Manuf. 1 (2019).
[20] E. Leveugle, D.S. Ivanov, L.V. Zhigilei, Photomechanical spallation of molecular and metal targets: molecular dynamics study, Appl. Phys. A-mater. 79 (2004) 1643–1655.
[21] J.X. Huang, K. Xu, J. Hu, D.D. Yuan, J. Li, J.Y. Qiao, S.L. Xu, Self-aligned plasmonic lithography for maskless fabrication of large-area long-range ordered 2d nanostructures, Nano Lett. 22 (2022) 6223–6228.
[22] J.X. Huang, K. Xu, S.L. Xu, X.W. Li, Q.H. Wei, Self-aligned laser-induced periodic surface structures for large-area controllable nanopatterning, Laser & Photonics Reviews 16 (2022).
[23] T. Apostolova, V. Kurylo, I. Gnilitskyi, Ultrafast laser processing of diamond materials: a review, Frontiers in Physics 9 (2021).
[24] J. Bonse, S. Graf, Maxwell meets Marangoni-a review of theories on laser-induced periodic surface structures, Laser Photon. Rev. 14 (2020).
[25] J. Bonse, S. Hohm, S.V. Kirner, A. Rosenfeld, J. Kruger, Laser-Induced Periodic Surface Structures-A Scientific Evergreen, Ieee J. Sel. Top. Quant. 23 (2017).
[26] Y. Jee, M.F. Becker, R.M. Walser, Laser-induced damage on single-crystal metal-surfaces, J. Opt. Soc. Am. B 5 (1988) 648–659.
[27] P.T. Mannion, J. Magee, E. Coyne, G.M. O'Connor, T.J. Glynn, The effect of damage accumulation behaviour on ablation thresholds and damage morphology in ultrafast laser micro-machining of common metals in air, Appl. Surf. Sci. 233 (2004) 275–287.
[28] Y. Dai, M. He, H.D. Bian, B. Lu, X.N. Yan, G.H. Ma, Femtosecond laser nanostructuring of silver film, Appl. Phys. A-mater. 106 (2012) 567–574.
[29] Z. Guosheng, P.M. Fauchet, A.E. Siegman, Growth of spontaneous periodic surface-structures on solids during laser illumination, Phys. Rev. B 26 (1982) 5366–5381.
[30] A.K. Jain, V.N. Kulkarni, D.K. Sood, J.S. Uppal, Periodic surface ripples in laser-treated aluminum and their use to determine absorbed power, J. Appl. Phys. 52 (1981) 4882–4884.
[31] A. Abdelmalek, B. Sotillo, Z. Bedrane, V. Bharadwaj, S. Pietralunga, R. Ramponi, E. H. Amara, S.M. Eaton, Origin of femtosecond laser induced periodic nanostructure on diamond, Aip Adv. 7 (2017).
[32] C.W. Xiong, C.Y. Ho, D.K. Qiao, Analysis of direct optical ablation and sequent thermal ablation for the ultrashort pulsed laser photo-thermal micromachining, Coatings 10 (2020).
[33] V.I. Konov, Laser in micro and nanoprocessing of diamond materials, Laser Photon. Rev. 6 (2012) 739–766.
[34] M. Sakakura, T. Tochio, M. Eida, Y. Shimotsuma, S. Kanehira, M. Nishi, K. Miura, K. Hirao, Observation of laser-induced stress waves and mechanism of structural changes inside rock-salt crystals, Opt. Express 19 (2011) 17780–17789.
[35] N. Bloembergen, Role of cracks, pores, and absorbing inclusions on laser-induced damage threshold at surfaces of transparent dielectrics, Appl. Optics 12 (1973) 661–664.
[36] P.H. Hasselman, Unified theory of thermal shock fracture initiation and crack propagation in brittle ceramics, J. Am. Ceram. Soc. 52 (1969) 600-+.
[37] V.L. Kuznetsov, I.L. Zilberberg, Y.V. Butenko, A.L. Chuvilin, B. Segall, Theoretical study of the formation of closed curved graphite-like structures during annealing of diamond surface, J. Appl. Phys. 86 (1999) 863–870.
[38] M.D. Shirk, P.A. Molian, A.P. Malshe, Ultrashort pulsed laser ablation of diamond, J. Laser Appl. 10 (1998) 64–70.
[39] M. Gertsvolf, H. Jean-Ruel, P.P. Rajeev, D.D. Klug, D.M. Rayner, P.B. Corkum, Orientation-dependent multiphoton ionization in wide band gap crystals, Phys. Rev. Lett. 101 (2008).
[40] H. Dachraoui, C. Oberer, U. Heinzmann, Femtosecond crystallographic experiment in wide-bandgap LiF crystal, Opt. Express 19 (2011) 2797–2804.